*Journal of Advanced Ceramics*
2023, **12**(5): 1046–1057
https://doi.org/10.26599/JAC.2023.9220737
ISSN 2226-4108
CN 10-1154/TQ

**Research Article**

# Dielectric barrier discharge-based defect engineering method to assist flash sintering

Xinhao Zhao[a], Nianping Yan[b], Yueji Li[a], Zikui Shen[c], Rongxia Huang[d], Chen Xu[e], Xuetong Zhao[f], Xilin Wang[a,*], Ruobing Zhang[a], Zhidong Jia[a]

[a]*Guangdong Engineering Technology Research Center of Power Equipment Reliability in Complicated Coastal Environments*, *Tsinghua Shenzhen International Graduate School*, *Tsinghua University*, *Shenzhen 518055*, *China*
[b]*State Grid Jiangxi Electric Power Research Institute*, *Nanchang 330096*, *China*
[c]*School of Electric Power Engineering*, *South China University of Technology*, *Guangzhou 510641*, *China*
[d]*School of Electromechanical Engineering*, *Guangdong University of Technology*, *Guangzhou 510006*, *China*
[e]*Institute of Materials*, *China Academy of Engineering Physics*, *Mianyang 621907*, *China*
[f]*School of Electrical Engineering*, *Chongqing University*, *Chongqing 400044*, *China*

Received: December 25, 2022; Revised: February 25, 2023; Accepted: February 26, 2023


**Abstract:** Oxygen vacancy $O_V$ plays an important role in a flash sintering (FS) process. In defect engineering, the methods of creating oxygen vacancy defects include doping, heating, and etching, and all of them often have complex processes or equipment. In this study, we used dielectric barrier discharge (DBD) as a new defect engineering technology to increase oxygen vacancy concentrations of green billets with different ceramics (ZnO, $TiO_2$, and 3 mol% yttria-stabilized zirconia (3YSZ)). With an alternating current (AC) power supply of 10 kHz, low-temperature plasma was generated, and a specimen could be treated in different atmospheres. The effect of the DBD treatment was influenced by atmosphere, treatment time, and voltage amplitude of the power supply. After the DBD treatment, the oxygen vacancy defect concentration in ZnO samples increased significantly, and a resistance test showed that conductivity of the samples increased by 2–3 orders of magnitude. Moreover, the onset electric field ($E$) of ZnO FS decreased from 5.17 to 0.86 kV/cm at room temperature (RT); while in the whole FS, the max power dissipation decreased from 563.17 to 27.94 W. The defect concentration and conductivity of the green billets for $TiO_2$ and 3YSZ were also changed by the DBD, and then the FS process was modified. It is a new technology to treat the green billet of ceramics in very short time, applicable to other ceramics, and beneficial to regulate the FS process.

**Keywords:** flash sintering (FS); ZnO; dielectric barrier discharge (DBD); oxygen vacancy $O_V$; defect engineering

* Corresponding author.
E-mail: wang.xilin@sz.tsinghua.edu.cn

## 1 Introduction

Flash sintering (FS) is an effective method for the rapid preparation of functional ceramic materials at low temperatures. It has the advantages of a fast-sintering speed and a high energy utilization rate [1]. Since Cologna *et al*. [2] proposed the concept of FS in 2010, this technology has been widely used in rapid-sintering research on various ceramic systems [3], including electron conducting ($MnCo_2O_4$ [4]), ion conducting (yttria-stabilized zirconia (YSZ) [2,5] and gadolinia-doped ceria [6]), insulating ($Al_2O_3$ [7]), and semiconducting (ZnO [8]) ceramics. ZnO ceramics are wide-band-gap semiconductor materials with a strong n-type conductivity. Two methods can be adopted to reduce the FS temperature of ZnO and even realize the FS at room temperature (RT, 25 ℃) without a heating furnace: increasing the conductivity of the specimen [9] and increasing the applied electric field (*E*) [10]. The formation of conductive defects and thermal runaway caused by Joule heating is often regarded as the main mechanisms to induce the FS of the YSZ [2] and ZnO [9,11]. Moreover, arc discharge and electric breakdown are regarded as the mechanisms of the FS of the YSZ [5] and ZnO [10], respectively. The mechanism, by which defects promote the FS, indicates that the onset conditions of the FS can be reduced by adjusting the defect concentration in the specimen. In Ref. [11], we used yellow ZnO powders with a high concentration of the oxygen vacancy defects as raw materials to reduce an onset alternating current (AC) electric field of the ZnO FS at RT to less than 0.51 kV/cm. This indicated that it is possible to reduce the onset electric field of the ZnO FS by increasing the concentration of the oxygen vacancy $O_V$ in raw powders. Furthermore, by doping iron into $SrTiO_3$, Shomrat *et al*. [12] introduced the oxygen vacancy defect, whose concentration depending on the doping concentration successfully reduced the onset temperature of the FS. Though some thermal treatment methods can introduce the oxygen vacancies into ZnO green billets, these methods usually spend long time in heating. We need a less-time and easier method to introduce the vacancies in ceramics.

Research on plasma deposition and etching semiconductor materials shows that the plasma can control the defect concentration in the materials. The plasma can introduce the defects by bombardment, etching, breaking chemical bonds, and lattice substitution of active particles, and it can also passivate the defects by the termination of dangling bonds [13]. There have been many promising applications using the plasma to introduce the defects, including graphene modification [14], realization of an electromagnetic-band-gap structure [15], chip manufacturing [16], adjustment of conductivity of transition metal halides [17], optimization of electrode materials [18], mechanoluminescence materials [19], and improvement of catalyst activity [20]. There have been lots of methods to control the defect concentrations of powders by the plasma, among which the dielectric barrier discharge (DBD) method has the prominent advantages of high efficiency and easy implementation. Furthermore, as a low-temperature plasma, the DBD plasma is not as challenging to produce as high-temperature plasma, and the DBD plasma can achieve high uniformity [21], which is beneficial for uniformly introducing the defects into the sample. With applications on ultroviolet (UV) lamp, ozone production, and film deposition, the DBD is an effective way to produce low-temperature plasma [21]. Two parallel dielectric plates are connected to two output terminals of the high-frequency AC or pulse power supply. By adjusting the output voltage, power supply, and atmosphere, the plasma composed of uniform filament discharge can be obtained in the space between the plates. Obviously, these materials after the plasma treatment will have useful performance changes or even be immediately used. In contrast, the green billets of the ceramics were just the intermediate state, and no plasma treatment in the billet was reported yet.

In this study, ZnO green billets were pretreated by the DBD plasma, which introduced high concentrations of the oxygen vacancy defects into the materials, thereby reducing the onset voltage of the ZnO FS at RT. In addition to ZnO, this defect control method using the DBD plasma can also be applied to other kinds of oxide ceramics that can produce rich point defects, like $TiO_2$ and 3YSZ.

## 2 Experimental

White pure ZnO powders with an average particle size of 200 nm (Anhui Sunrise Stationery Co., Ltd., China) was used. 5 wt% polyvinyl alcohol (PVA) organic binder and ZnO powders were mixed and ground for 10 min. A dog-bone-shaped sample was prepared by uniaxially pressing under a pressure of 300 MPa for 2 min. The middle strip of sample was 13 mm long, 3.3 mm wide, and 1.7 mm high. The sample was

heated at 600 ℃ for 1 h to remove the organic binder. The relative density of the ZnO green body was approximately 65%. Other powders used were 3YSZ with an average particle size of 30 nm (Nanjing Mission New Materials Co., Ltd., China) and anatase $TiO_2$ with an average particle size of 50 nm (Guangzhou Metallurgy Industry Co., Ltd., China). Dog-bone-shaped 3YSZ and $TiO_2$ samples were prepared using a method similar to that of ZnO.

A DBD device (Fig. 1) is used to treat the ZnO samples with an air-gap width of 3 mm for plasma generation. A voltage regulator (CHNT TDGC 2-1, Zhejiang Zhengtai Electric Technology Co., Ltd., China) was connected in series with a low-temperature plasma experimental power supply (CTP-2000K, Nanjing Suman Electronics Co., Ltd., Jiangsu, China) to generate a high-frequency AC. According to the experiment, the most uniform plasma was produced when the output voltage amplitude of the power supply was 5 kV. In this study, the power supply's output voltage frequency was 10 kHz, the voltage amplitude ($U_m$) was 5 kV, and the effective value of the current was 80 mA, which was measured using an oscilloscope (TDS1012B-SC, Tektronix (CHINA) Co., Ltd., China).

Two different atmospheres were used in the experiment: One is air, and the other is an atmosphere of 0.01 atm air and 0.59 atm Ar. A small amount of air was mixed in gas because the Ar atmosphere in a box was obtained by pumping air to form vacuum, and then filling the box with Ar, while the minimum air pressure obtained in the box was 0.01 atm. Six samples treated using the same method were recorded as A1–A6. Six samples without the DBD treatment were recorded as B1–B6 for the contrast group. Four samples treated with the DBD plasma for 20 min in atmospheric air were recorded as C1–C4. The samples were taken out when the sample temperature dropped to RT after being kept in the box for 30 min after the DBD treatment. The DBD treatment was conducted on the 3YSZ and $TiO_2$ samples in the same manner as ZnO.

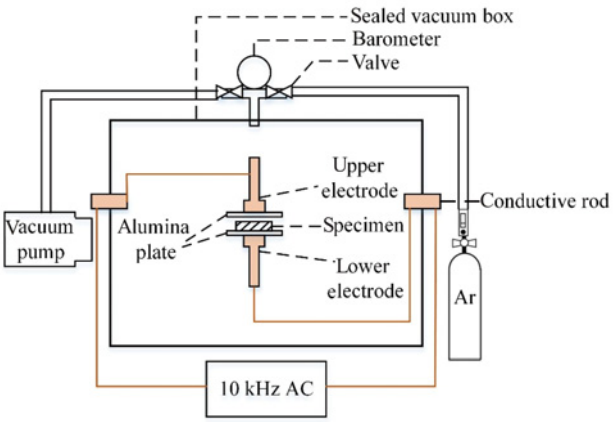


**Fig. 1** Schematic of DBD device.

Before the FS, the two ends of the dog-bone-shaped sample were covered with a silver paste as electrodes to improve electrical contact. Both ends of the sample were wrapped with a platinum (Pt) wire and connected to an AC power supply (50 Hz; YDTW 100/50, Yangzhou Xinyuan Electric Co., Ltd., China) through a 7 kΩ current-limiting resistor in series. A data acquisition card (USB-6210, National Instruments Corp., USA) with the highest sampling rate of 5 kHz was used to measure voltage and current. The sampling rate of the voltage and current in this study was 1 kHz. The sample was placed in air on an alumina plate. The voltage was manually increased until a flash event occurred, and the power supply was turned off after maintaining a stable current for 60 s. Experiments were conducted at RT (25 ℃).

A multimeter (UNI-T UT61E, UNI-TREND Technology (CHINA) Co., Ltd., China) and a digital sourcemeter (Keithley 2470, Keithley Instruments, Inc., USA) were used to measure resistance of the samples, and then the conductivity was calculated accordingly. Before measuring the resistance of the sample, the silver paste on both ends of the sample as the electrode was applied, and the sample to output ports of the multimeter or sourcemeter with wires was connected. The measurement for 5 times by each method was repeated, the average value of the ten results was taken, and the conductivity according to the size of the middle strip of the sample was calculated. The density of the sintered samples were measured using Archimedes drainage method. Weights of the samples were measured by a digital balance (WT-B, Hangzhou Wante Weighing Co., Ltd., China). A beaker with water on the balance was placed, the sample with a thin wire was wrapped and immersed completely in water, the change in digital balance indication was read, and the volume of the sample was calculated. A high-speed camera (Phantom V2012, AMETEK Inc., USA) was used to capture snapshots of the samples during the FS process at a frequency of 3 kHz. A scanning electron microscope (SEM; SU8010, Hitachi Co., Ltd., Japan) was used to detect surface morphologies of the samples. An X-ray photoelectron spectrometer (XPS; PHI 5000 Versa Probe II, ULVAC- PHI, Inc., Japan) was used to study

chemical states of elements in the samples. Point defects in the samples were detected using an electron paramagnetic resonance (EPR) spectrometer (A300, Bruker (Beijing) Scientific Technology Co. Ltd., China).

## 3 Results and discussion

The oxygen vacancy defect of the ZnO samples with (A1) and without (B1) DBD treatment was analyzed via X-ray photoelectron spectroscopy (XPS) and EPR spectroscopy. Figure 2(a) shows O 1s XPS profile of the untreated sample (w/o DBD) and the inside (DBD_inside) and surface (DBD_surface) of the sample after the DBD treatment in almost pure Ar. For the inside of the sample, we cut the sample in half from the middle and chose the center point of the cross section for the XPS test. The O 1s spectra were classified into three peaks, $O_L$, $O_V$, and $O_A$ [22], representing lattice oxygen, oxygen vacancy, and adsorbed oxygen, respectively. The $O_A$ signal of the untreated sample was the strongest, whereas the oxygen vacancy content of the sample after the DBD treatment significantly increased compared with that of the untreated one. The surface and inside of the DBD-treated sample showed similar oxygen vacancy contents. In addition, the DBD treatment made the small amount of $O_A$ in the sample almost disappear completely. The XPS results show that the Ar DBD treatment uniformly introduced a high concentration of oxygen vacancy defects both on the surface and inside ZnO. On the contrary, the DBD treatment in air had little effect on proportion of three existing forms of oxygen element (Fig. 2(b)), which indicated that the Ar atmosphere was much better than air for the DBD treatment in this study. The EPR can be used to characterize the contents of paramagnetic oxygen vacancy defects. Figure 3(a) shows the EPR spectra of the ZnO sample with (DBD) and without DBD

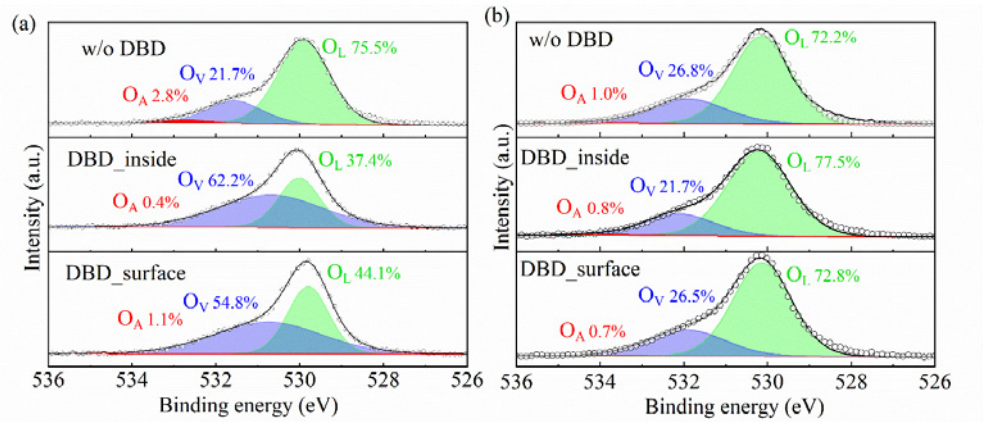


**Fig. 2** O 1s XPS profiles of sample without DBD treatment (w/o DBD) and inside (DBD_inside) and surface (DBD_surface) of sample with DBD treatment in atmospheres of (a) almost pure Ar and (b) air.

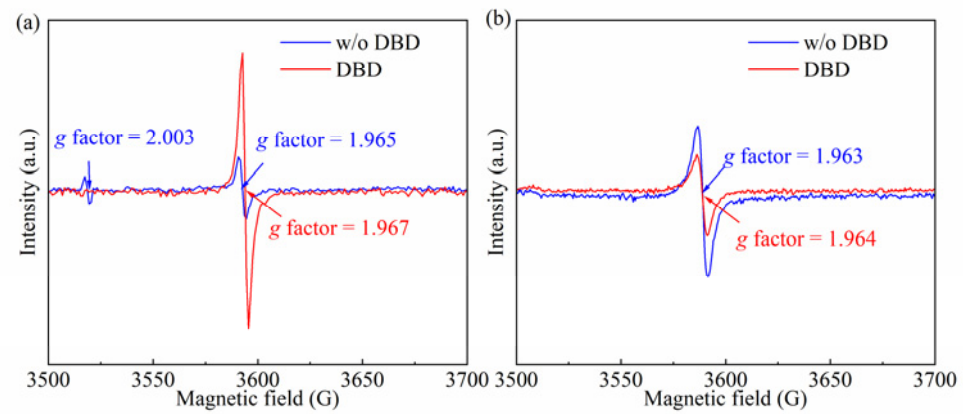


**Fig. 3** EPR spectra of ZnO sample with (DBD) and without (w/o DBD) DBD treatment in atmospheres of (a) almost pure Ar and (b) air.

treatment (w/o DBD) in an almost pure Ar atmosphere. Two bimodal signals are observed in the spectra of the untreated sample. The bimodal signal at $g$ = 1.965 ($g$ is the factor of the EPR test related to magnetic field strength) originated from single-ionized oxygen vacancies ($V_O^+$), and the bimodal signal at $g$ = 2.003 originated from zinc vacancies ($V_{Zn}^{2-}$) [23]. The intensity of the signal representing oxygen vacancies increased significantly after the sample was the DBD treated, whereas the signal representing $V_{Zn}^{2-}$ almost disappeared. The EPR results show that the DBD treatment considerably increased the concentration of the oxygen vacancies in the ZnO samples and reduced the concentration of $V_{Zn}^{2-}$. Consistent with the XPS results, the EPR results also showed that the concentration of the oxygen vacancy in the sample did not increase, but slightly decreased after the DBD treatment in air (Fig. 3(b)).

It can be concluded from the above results that the DBD treatment increased the concentration of the oxygen vacancies in ZnO. It is necessary to consider the mechanism of how the plasma penetrated into the ZnO green billets and introduced the oxygen vacancies. Ra *et al*. [24] showed that $Ar^+$ in the Ar plasma treatment could sputter oxygen atoms in ZnO nanowires within several nanometers, thereby introducing the oxygen vacancies. The energy of $Ar^+$ in the Ar plasma is typically several or tens of electron volts [24,25]. Correspondingly, the formation of the oxygen vacancy defects in ZnO can be of the order of several electron volts under various conditions [26], which makes it possible to introduce the oxygen vacancy defects into ZnO using the Ar plasma. Reference [27] shows that the plasma can only introduce the oxygen vacancies within a few nanometers of the surface of the ZnO sample. However, this study shows a different result: the DBD plasma introduced the oxygen vacancies into the 1.7 mm-thick sample rather than just the surface. This could be explained by the unique atmosphere of the DBD treatment and the porous macrostructure of the sample. First, high-purity argon was used as the atmosphere of the DBD. The partial pressure of oxygen was approximately 0.0021 atm, whereas the total pressure was 0.6 atm. The extremely low oxygen partial pressure and low total pressure make the oxygen in the sample more inclined to separate from the bulk. Second, the target of the DBD treatment was porous green ZnO billets. It has a porous structure, and many flow paths connect and run through the surface of the sample. Figure 4 shows the mechanism of the formation of the oxygen vacancies by the Ar DBD plasma treatment. The oxygen atoms sputtered from the lattice escaped from the bulk sample in the form of oxygen molecules, and the oxygen vacancies were formed in the original positions of the sputtered oxygen atoms. For the charge compensation, when each oxygen ion with two negative charges changed into an oxygen vacancy with one positive charge in the lattice, three electrons were left and reduced zinc ions. On the one hand, Refs. [28,29] show that higher porosity, better pore connectivity, and larger pore size promote the plasma penetration into porous materials. Therefore, the porous structure of the ZnO green billet enabled the penetration of high-energy electrons, ions such as $Ar^+$, and other active particles from the surface of the sample to the interior. On the other hand, the porous ZnO green body, as the object of the DBD plasma treatment, also participated in the generation of the discharge as a dielectric layer. The electric field in the pores of the porous materials may be distorted and significantly increase numerically [30]. When the local electric field exceeds the breakdown electric field of the gas atmosphere, micro-discharged plasma is generated in the pores. In conclusion, the penetration depth of the Ar plasma into the ZnO green billet depends on the distribution of the pores, whereas the penetrated $Ar^+$ tends to introduce the oxygen vacancies within a few nanometers under a grain surface by sputtering and breaking Zn–O bonds, according to Ref. [24].

The electrical properties of the samples A2, B2, and C1 are characterized and listed in Table 1. The conductivity of the ZnO sample improved by approximately two orders of magnitude after the DBD treatment. The effect of

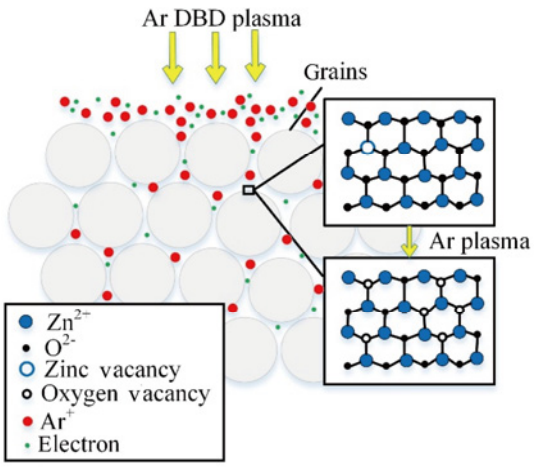


**Fig. 4** Mechanism of formation of oxygen vacancies by Ar DBD plasma treatment.

**Table 1 Conductivities of 1.7 mm-thick samples A2, B2, and C1 and 2.4 mm-thick samples with and without DBD treatment**

| 1.7 mm sample | A2 | | B2 | | C1 | |
|---|---|---|---|---|---|---|
| Conductivity (μS/cm) | 100.75±5.00 | | 1.78±0.10 | | 1.82±0.10 | |
| 2.4 mm sample | DBD | | | | Average | w/o DBD |
| Conductivity (μS/cm) | 7379.9±200.0 | 1482.3±40.0 | 5666.2±140.0 | 675.2±20.0 | 3799.4±200.0 | 2.5±0.1 |

the concentration of the oxygen vacancies on the conductivity of ZnO was investigated. The oxygen vacancies have prominent donor properties. It tends to provide electrons to a conduction band, which increases the n-type conductivity of ZnO [31]. It has been confirmed that the content of $V_O^+$ in ZnO positively correlates with the conductivity [32]. The atmosphere is an essential factor affecting the effect of the DBD treatment. As shown in Table 1, the conductivity of the sample C1 was close to that of the sample B2, indicating that the DBD treatment in atmospheric air hardly affected the conductivity of the sample. The effect of the DBD treatment in 0.59 atm Ar and 0.01 atm air was much better than that in atmospheric air.

To prove that the DBD plasma can penetrate thicker samples, 2.4 mm-thick ZnO samples were prepared as a control. Except here, the samples discussed in the rest of this paper were all 1.7 mm-thick. The 69% relative density of the 2.4 mm-thick samples is close to 65% of the 1.7 mm-thick samples used previously. According to Table 1, the DBD pretreatment with the same parameters as the 1.7 mm-thick samples increased the conductivity of the 2.4 mm-thick samples by three orders of magnitude. The results showed that increasing the sample thickness did not affect the effect of the DBD treatment. In contrast, the treatment effect of thicker samples was better, because the resistance test was carried out in air, and thin samples were more likely to absorb oxygen from air through their surfaces. In addition, Table 1 clearly shows that the DBD treatment increased the conductivity value of the samples randomly, whereas the conductivity of different samples after the same treatment showed a large dispersion. This was because the numbers and positions of micro-discharges in the samples were random during the DBD treatment. Considering the dispersion, the effect of the DBD treatment was still obvious, because the conductivity of each treated sample was much higher than that of the untreated sample.

The treatment duration and amplitude of the output voltage of the power supply also affected the treatment results. Figure 5(a) depicts the variety in the sample resistivity ($\rho$) after the DBD plasma treatment for various duration. All samples did not shrink after the treatment, and the density remained unchanged. The $\rho$ of the samples decreased with the increased treatment time. This indicates that the longer the treatment time, the higher the oxygen vacancy concentration was introduced into the sample. The rise of the conductivity reached saturation at 20 min. Therefore, considering saving time in the treatment, the optimal treatment time was 20 min. As shown in Fig. 5(b), there was no change in $\rho$ when $U_m$ varied from 0 to 3 kV because the DBD plasma was not generated until $U_m$ achieved

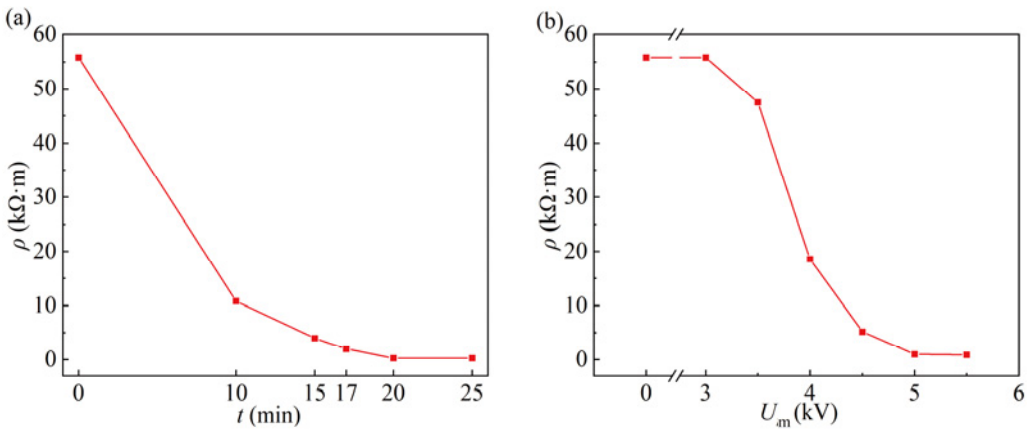


**Fig. 5** $\rho$ of samples after DBD treatment (a) at different treatment time ($t$) when $U_m$ = 5 kV and (b) at different $U_m$ when $t$ was 20 min in an atmosphere of 0.01 atm air and 0.59 atm Ar.

3.5 kV. The $\rho$ rapidly decreased when $U_m$ was increased from 3 to 5 kV, and the concentration of the introduced oxygen vacancies reached saturation. Therefore, to reduce the heating of the sample and the cooling time, the best $U_m$ was 5 kV in this air-gap distance. In addition, the DBD treatment mentioned in the rest of this study used the optimal parameters mentioned in Section 2.

The effect of the DBD treatment on the conductivity of 3YSZ and $TiO_2$ was also investigated to demonstrate the versatility of the defect engineering method used in this study. Figure 6 shows that the DBD treatment significantly increased the electrical conductivity of all three materials to different degrees, and the density of the samples did not change after the treatment. The conductivities of these three materials are closely related to the concentration of the oxygen vacancy. For n-type semiconductor materials such as ZnO and $TiO_2$, the concentration of the oxygen vacancies is positively correlated with n-type conductivity because the oxygen vacancies are donor defects and can provide free electrons. For 3YSZ and other oxygen ionic conductors, the oxygen vacancies are main carriers, so the oxygen vacancy concentration is also positively related to the ionic conductivity. In addition, the conductivities of 3YSZ and $TiO_2$ can be increased by introducing the oxygen vacancies into the materials [33,34]. Moreover, using the DBD plasma treatment, Li *et al*. [35] have successfully introduced the oxygen vacancy defects into $TiO_2$ nanosheets. Our study expands the scope of the DBD plasma treatment for defect engineering from the nanometer scale to the millimeter scale, owing to the porous structure of the green body. The experimental results of ZnO, 3YSZ, and $TiO_2$ indicate that the DBD defect engineering method proposed in this paper can be applied to introducing the oxygen vacancy defects into porous metal oxides, provided that the substance to be treated easily generates oxygen vacancies.

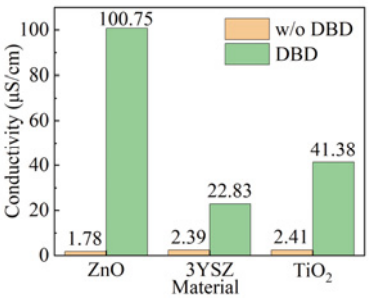


**Fig. 6** Electrical conductivity comparison of ZnO, 3YSZ, and $TiO_2$ green bodies with (DBD) and without (w/o DBD) DBD treatment.

The effect of the DBD pretreatment on the initial FS stage of ZnO was studied comprehensively through experiments. Figure 7 shows the changes in the current density ($J$) and $E$ of the samples A2 and B2 during the entire process of the FS and around the onset instant of the flash event. The results for the samples A3–A6 and B3–B6 were similar to those for A2 and B2, respectively. The sample A2 began to flash when the electric field reached 0.86 kV/cm. During the subsequent 3.2 s (15.4–18.6 s), the electric field on the sample A2 gradually decreased to 0.12 kV/cm. Simultaneously, the current density increased from 0.61 to 15.81 mA/mm$^2$. Notably, in this stage, the electric field decreases gradually. In the middle 1 s (17–18 s), the electric field decreased rapidly from 0.79 to 0.16 kV/cm. As the current density of 15.81 mA/mm$^2$ was insufficient to sinter the ZnO sample to a nearly full density, the current density was increased to 85 mA/mm$^2$. The parameter changes in the sample B2 are similar to those previously reported in Ref. [10]. A flash event

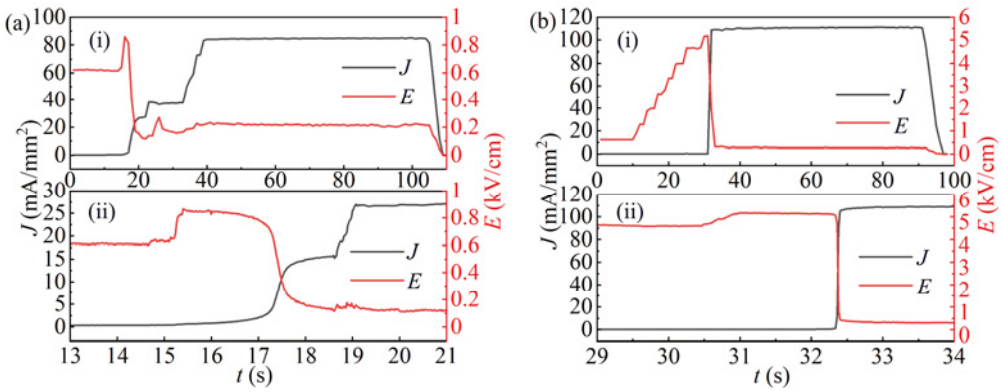


**Fig. 7** $J$ and $E$ of samples (a) A2 and (b) B2: (i) in the whole FS process and (ii) around flash event.

occurred when the electric field reached 5.17 kV/cm. Then the electric field decreased from 5.07 to 0.44 kV/cm in 0.06 s (32.34–32.4 s), whereas the current density increased from 1.14 to 104.74 mA/mm$^2$. The current density of B2 during the stable FS stage was 110 mA/mm$^2$.

The DBD pretreatment made the onset electric field of the sample A2 (0.86 kV/cm) significantly lower than that of the sample B2 (5.17 kV/cm). The results of the five groups of repeated comparative experiments (Table 2) show that the reduction in the onset electric field of the FS by the DBD treatment was not coincidental. The onset electric fields of different samples were dispersive because the conductivities of different samples were dispersive after the DBD treatment. The results show that the DBD treatment significantly reduced the rate of the change of the electric field and current of the sample when the flash event occurred, which made the transition process from an incubation period to a stable period of FS gentler, and reduced probability of FS failure. The onset electric fields of the FS for the samples C1–C4 treated with the DBD in atmospheric air are listed in Table 2 for comparison. Compared with those of B2–B6, the onset electric fields of C1–C4 did not decrease significantly. The DBD atmosphere of C1–C4 was rich in oxygen, which is not conducive to introducing the oxygen vacancies into ZnO. Thus, in this study, Ar is a better atmosphere for the DBD treatment than air.

Figure 8 shows snapshots of the samples A2 and B2 during the FS. A high-speed camera recorded the phenomenon of the samples during the FS. The snapshots of the samples A3–A6 and B3–B6 were similar to those of A2 and B2, respectively. The FS behavior of the sample A2 was similar to that of yellow zinc oxide with a high concentration of the oxygen vacancies, as previously reported in Ref. [11].

**Table 2 Onset electric fields of samples treated with almost pure Ar DBD plasma (A2–A6), without DBD plasma (B2–B6), and with air DBD plasma (C1–C4)**

(Unit: kV/cm)

| A2 | A3 | A4 | A5 | A6 | Average |
|---|---|---|---|---|---|
| 0.86 | 2.50 | 2.45 | 3.12 | 1.73 | 2.14 |
| B2 | B3 | B4 | B5 | B6 | Average |
| 5.17 | 6.63 | 6.12 | 4.62 | 5.40 | 5.60 |
| C1 | C2 | C3 | C4 | | Average |
| 5.33 | 6.71 | 4.45 | 4.22 | | 5.18 |

With an increase in the current density, the luminescence of the sample body became stronger. No apparent discharge phenomenon was observed on the sample surface, indicating that the thermal runaway process attributed to Joule heating may be primary mechanism for the FS of the sample A2. The FS behavior of the sample B2 was similar to the previously reported rapid occurrence of arc-induced FS [36]. Initially, prominent light spots appeared on the sample surface, and then a periodic discharge occurred at the junction between the electrode and the sample surface, similar to the surface flashover, and a weak arc was observed above the sample. After several seconds, the discharge disappeared, and the sample body emitted a bright light. The light intensity emitted by the thermal radiation of the sample B2 is greater than that of the sample A2, indicating that the temperature of the sample B2 is higher than that of the sample A2. The snapshot shows that periodic discharge and heating effect of the arc on the sample lead to the FS of B2. The DBD treatment changed the primary ignition mechanism of ZnO flashover from the heating effect of arc discharge to thermal runaway attributed to Joule heating. Figure 9 shows power consumption changes in the samples A2 and B2 near the flash event. The power consumption of the sample A2 slowly increased from 3.83 to 27.94 W within 2.04 s (2.4–4.44 s), and

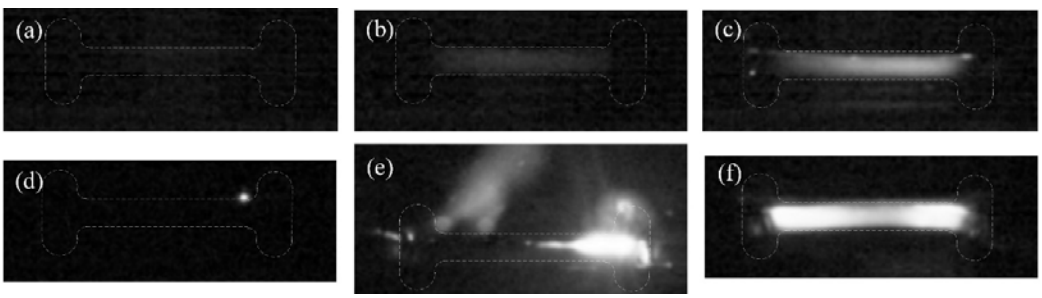


**Fig. 8** Snapshots for samples (a–c) A2 and (d–f) B2 during FS: (a) 0 s, (b) 3.00 s, (c) 13.70 s, (d) 0 s, (e) 0.06 s, and (f) 5.88 s after beginning of flash event.

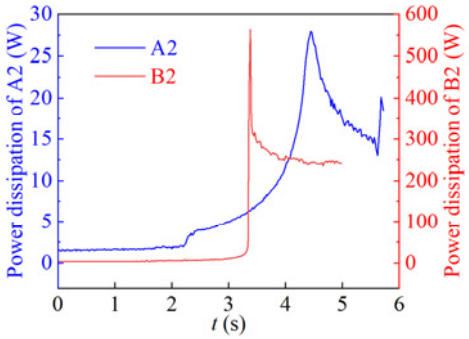


**Fig. 9** Power dissipation of samples A2 and B2 around flash event.

decreased to 13.51 W in the subsequent 1.16 s. In contrast, the power consumption of the sample B2 increased rapidly from 42.37 to 563.17 W within just 0.04 s (3.34–3.38 s), and decreased to 334.88 W in the subsequent 0.02 s. The change in the power consumption of the samples A2 and B2 is consistent with the change in the temperature, as shown in the snapshot; that is, the power consumption of the sample A2 at the beginning of the FS was significantly lower than that of the sample B2, and Joule heating rate was also significantly slower than that of the sample B2. In addition, the sample B2 exhibited a more pronounced power spike. The difference in the conductivity attributed to different concentrations of the oxygen vacancies was the direct reason for the different onset electric fields and FS behavior of the samples A2 and B2. The sample A2 was more conductive than the sample B2; therefore, it could begin to flash at a lower electric field. In addition, the higher bulk conductivity of A2 caused the current to flow through the sample from the beginning of the FS rather than the flashover discharge on the surface that occurred with B2.

The density of the sintered samples A2 and B2 were characterized. The relative density of the sintered samples A2 and B2 measured by Archimedes method were 98.5% and 95.5%, respectively. Figure 10 shows SEM images of the sintered samples A2 and B2. Although the current density of the sample A2 in a stable stage was lower than that of the sample B2, the sintered sample A2 was significantly denser than the sample B2, which is consistent with the density measurement results. This is because of the current flowing through the sample A2 from the beginning of the FS, whereas the arc discharge that existed on the surface of the sample B2 for a long time made the actual current density flowing through the sample B2 lower than the measured one. In addition, the inherently high concentration of the charged oxygen vacancy defects in A2 promoted densification. In addition, the grain size of the sample A2 was uniformly distributed in the whole sample, whereas the sample B2 showed an apparent gradient of the grain size from the surface to the center of the cross section. This may be because the oxygen vacancies introduced in the sample A2 improved the uniformity of the current distribution. In addition, the sample B2 had a higher temperature during the stable stage of the FS, so the temperature difference between the sample B2 and the surrounding air was greater; therefore, the heat dissipation effect from the surface of the sample B2 became stronger. This caused the surface temperature of the sample B2 to be much lower than the internal temperature, resulting in an uneven grain size distribution. In summary, the DBD pretreatment made the grain size distribution of the sintered sample A2 more uniform.

The DBD treatment increased the conductivity of the 3YSZ and $TiO_2$ green billets, and changed their electrical behavior at the beginning of the FS at RT (Figs. 11 and 12). For these two kinds of ceramics, the FS process started with the heating of the sample by the arc on the surface of the sample, which gradually increased the conductivity of the sample, and finally, the current path was transferred from above the sample to inside the sample. Unlike the case of ZnO, the DBD treatment did not eliminate the arc generated on the surface of the 3YSZ and $TiO_2$ samples at the beginning of the FS, although their conductivities had already increased significantly. This may be because the electric breakdown in the 3YSZ and $TiO_2$ samples was

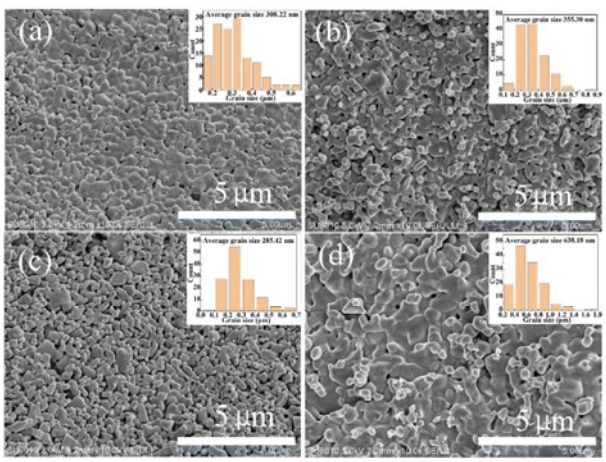


**Fig. 10** SEM images of (a) surface and (b) cross section of sample A2 and (c) surface and (d) cross section of sample B2.

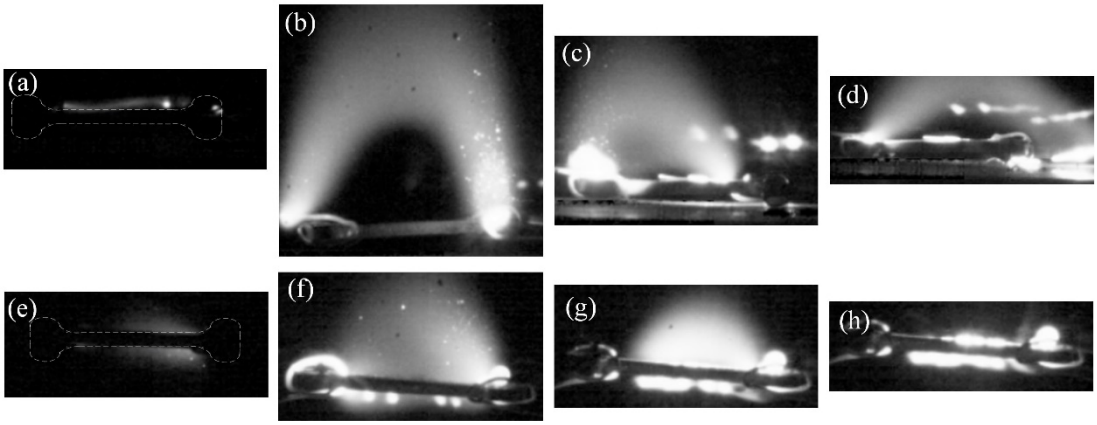


**Fig. 11** Snapshots for 3YSZ samples: (a) 0 s, (b) 0.75 s, (c) 5.81 s, and (d) 9.17 s after beginning of FS for sample without DBD treatment; (e) 0 s, (f) 1.79 s, (g) 7.28 s, and (h) 7.40 s for sample with DBD treatment.

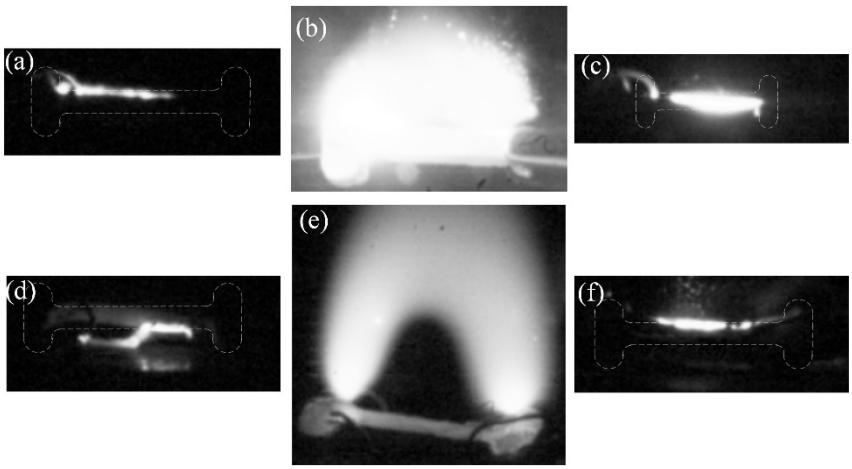


**Fig. 12** Snapshots for $TiO_2$ samples: (a) 0 s, (b) 0.24 s, and (c) 0.72 s after beginning of FS for sample with DBD treatment; (d) 0 s, (e) 0.74 s, and (f) 1.37 s for sample without DBD treatment.

considerably more difficult to occur than that in ZnO; therefore, the surface flashover tended to appear. In addition, the increase in the conductivities by the DBD treatment on the 3YSZ and $TiO_2$ samples was lower than that of ZnO, which made the 3YSZ and $TiO_2$ samples after the DBD treatment still tend to have the surface flashover first. However, the effect of the DBD treatment on the FS was still apparent. First, the arc above the DBD-treated 3YSZ sample disappeared 7.40 s after its appearance. However, the arc continued to exist above the untreated 3YSZ sample for 9.17 s until the Pt wire fused owing to long burning time of the high-temperature arc. The duration of the arc above the $TiO_2$ sample was also reduced from 1.37 to 0.72 s. Because the sample became more conductive after the DBD treatment, the current could be transferred from above the sample to the inside more quickly, which also prevented the failure of the experiment caused by Pt wire fusing. Second, for the untreated 3YSZ and $TiO_2$ samples, the arc above them floated at a certain distance above the sample for a long proportion of its existing time. However, for the 3YSZ and $TiO_2$ samples after the DBD treatment, because the sample surface became more conductive, the arc was attached to the sample surface. This increased the heating effect of the arc on the sample and accelerated the disappearance of the arc.

## 4 Conclusions

This is the first report of the DBD treatment in ceramic green billets that the DBD plasma introduced many oxygen vacancy defects in the ZnO green billet samples in short time, thereby increasing their conductivities. The high concentration of the oxygen

vacancies significantly reduced the onset electric field of the FS at RT, and changed the primary mechanism of the FS from heating by periodic arc discharge to thermal runaway attributed to Joule heating. The effect of the DBD treatment was affected by atmosphere, treatment time, and voltage amplitude of the power supply. The DBD pretreatment had different effects on different oxide ceramics, such as ZnO, 3YSZ, and $TiO_2$, and affected their behavior during the initial stage of the FS to different degrees. Compared with other defect engineering methods, the DBD technology had many advantages, such as simple equipment, controllability of the treatment parameters, suitability to all atmospheres and ceramics, and short time. The DBD plasma pretreatment method proposed in this study to regulate the defects in the green body of ceramics provides an effective assistance for many other ceramic systems that can easily induce defects. Future research will focus on the detection and regulation of the physical and chemical properties of the plasma, the influence of the pore distribution of the materials to be treated on the treatment effect, and the expanded application of the proposed defect engineering method to metal oxides, metal-oxide mixtures, and other material systems.

## Acknowledgements

This work was supported by the National Natural Science Foundation of China (No. 52077118), the Guangdong Basic and Applied Basic Research Foundation (No. 2021A1515011778), and State Key Laboratory of Power System Operation and Control, Tsinghua University (No. SKLD22KM01).

## Declaration of competing interest

The authors have no competing interests to declare that are relevant to the content of this article.

## References

[1] Biesuz M, Sglavo VM. Flash sintering of ceramics. *J Eur Ceram Soc* 2019, **39**: 115–143.

[2] Cologna M, Rashkova B, Raj R. Flash sintering of nanograin zirconia in < 5 s at 850 ℃. *J Am Ceram* Soc 2010, **93**: 3556–3559.

[3] Zhou HY, Li X, Zhu YC, *et al*. Review of flash sintering with strong electric field. *High Volt* 2022, **7**: 1–11.

[4] Gaur A, Sglavo VM. Flash-sintering of $MnCo_2O_4$ and its relation to phase stability. *J Eur Ceram Soc* 2014, **34**: 2391–2400.

[5] Zhu YC, Zhou HY, Huang RX, *et al*. Gas-discharge induced flash sintering of YSZ ceramics at room temperature. *J Adv Ceram* 2022, **11**: 603–614.

[6] Hao XM, Liu YJ, Wang ZH, *et al*. A novel sintering method to obtain fully dense gadolinia doped ceria by applying a direct current. *J Power Sources* 2012, **210**: 86–91.

[7] Cologna M, Francis JSC, Raj R. Field assisted and flash sintering of alumina and its relationship to conductivity and MgO-doping. *J Eur Ceram Soc* 2011, **31**: 2827–2837.

[8] Dargatz B, Gonzalez-Julian J, Guillon O. Effect of electric field and atmosphere on the processing of nanocrystalline ZnO. In: Proceedings of the Oxide-based Materials and Devices V, San Francisco, USA, 2014, **8987**: 89871H.

[9] Nie JY, Zhang YY, Chan JM, *et al*. Water-assisted flash sintering: Flashing ZnO at room temperature to achieve ~98% density in seconds. *Scripta Mater* 2018, **142**: 79–82.

[10] Liu JM, Li X, Wang XL, *et al*. Alternating current field flash sintering 99% relative density ZnO ceramics at room temperature. *Scripta Mater* 2020, **176**: 28–31.

[11] Wu AX, Yan ZY, Wang XL, *et al*. A versatile defect engineering strategy for room-temperature flash sintering. *J Adv Ceram* 2022, **11**: 1172–1178.

[12] Shomrat N, Baltianski S, Dor E, *et al*. The influence of doping on flash sintering conditions in $SrTi_{1-x}Fe_xO_{3-\delta}$. *J Eur Ceram Soc* 2017, **37**: 179–188.

[13] Liu FZ, Leung YH, Djurišić AB, *et al*. Effect of plasma treatment on native defects and photocatalytic activities of zinc oxide tetrapods. *J Phys Chem C* 2014, **118**: 22760–22767.

[14] Yue ZJ, Seo DH, Ostrikov K, *et al*. Defects induced ferromagnetism in plasma-enabled graphene nanopetals. *Appl Phys Lett* 2014, **104**: 092417.

[15] Lo J, Sokoloff J, Callegari T, *et al*. Reconfigurable electromagnetic band gap device using plasma as a localized tunable defect. *Appl Phys Lett* 2010, **96**: 251501.

[16] Ghica C, Nistor LC, Vizireanu S, *et al*. Skin layer defects in Si by optimized treatment in hydrogen RF plasma. *Plasma Process Polym* 2010, **7**: 986–991.

[17] Islam MR, Kang N, Bhanu U, *et al*. Tuning the electrical property via defect engineering of single layer $MoS_2$ by oxygen plasma. *Nanoscale* 2014, **6**: 10033–10039.

[18] Zhu JF, Chen J, Xu H, *et al*. Plasma-introduced oxygen defects confined in $Li_4Ti_5O_{12}$ nanosheets for boosting lithium-ion diffusion. *ACS Appl Mater Interfaces* 2019, **11**: 17384–17392.

[19] Cai YY, Liu SB, Zhao L, *et al*. Delayed stress memory by $CaAl_2O_4$:$Eu^{2+}$ mechanoluminescent phosphor with defect engineering regulation. *J Adv Ceram* 2022, **11**: 1319–1329.

[20] Wang Y, Arandiyan H, Chen XJ, *et al*. Microwave-induced plasma synthesis of defect-rich, highly ordered porous

phosphorus-doped cobalt oxides for overall water electrolysis. *J Phys Chem C* 2020, **124**: 9971–9978.
[21] Duan X, He F, Ouyang J. Uniformity of a dielectric barrier glow discharge: Experiments and two-dimensional modeling. *Plasma Sources Sci Technol* 2012, **21**: 015008.
[22] Lei J, Liu W, Jin Y, *et al*. Oxygen vacancy-dependent chemiluminescence: A facile approach for quantifying oxygen defects in ZnO. *Anal Chem* 2022, **94**: 8642–8650.
[23] Liu MH, Chen YW, Lin TS, *et al*. Defective mesocrystal ZnO-supported gold catalysts: Facilitating CO oxidation via vacancy defects in ZnO. *ACS Catal* 2018, **8**: 6862–6869.
[24] Ra HW, Choi KS, Ok CW, *et al*. Ion bombardment effects on ZnO nanowires during plasma treatment. *Appl Phys Lett* 2008, **93**: 033112.
[25] Liu F, Huang G, Ganguly B. Plasma excitation dependence on voltage slew rates in 10–200 torr argon–nitrogen gas mixture DBD. *Plasma Sources Sci Technol* 2010, **19**: 045017.
[26] Lin CJ, Zhu ZZ. First-principles studies on the formation energy of oxygen vacancies in ZnO. *J Xiamen Univ (Nat Sci)* 2017, **56**: 486–491. (in Chinese)
[27] Gurylev V, Perng TP. Defect engineering of ZnO: Review on oxygen and zinc vacancies. *J Eur Ceram Soc* 2021, **41**: 4977–4996.
[28] Wang CX, Du M, Qiu YP. Influence of pore size on penetration of surface modification into woven fabric treated with atmospheric pressure plasma jet. *Surf Coat Tech* 2010, **205**: 909–914.
[29] Rakhimova TV, Lopaev DV, Mankelevich YA, *et al*. Interaction of F atoms with SiOCH ultra-low-*k* films: I. Fluorination and damage. *J Phys D Appl Phys* 2015, **48**: 175203.
[30] Zhu M, Hu SY, Zhang YH, *et al*. Plasma propagation in single-particle packed dielectric barrier discharges: Joint effects of particle shape and discharge gap. *Plasma Sci Technol* 2022, **24**: 065401.
[31] Janotti A, van de Walle CG. Native point defects in ZnO. *Phys Rev B* 2007, **76**: 165202.
[32] Vanheusden K, Warren WL, Seager CH, *et al*. Mechanisms behind green photoluminescence in ZnO phosphor powders. *J Appl Phys* 1996, **79**: 7983–7990.
[33] Yang SH, Li Y, Sun J, *et al*. Laser induced oxygen-deficient $TiO_2$/graphene hybrid for high-performance supercapacitor. *J Power Sources* 2019, **431**: 220–225.
[34] Carvalho SGM, Muccillo ENS, Muccillo R. Electrical behavior and microstructural features of electric field-assisted and conventionally sintered 3 mol% yttria-stabilized zirconia. *Ceramics* 2018, **1**: 3–12.
[35] Li BB, Zhao ZB, Zhou Q, *et al*. Highly efficient low-temperature plasma-assisted modification of $TiO_2$ nanosheets with exposed {001} facets for enhanced visible-light photocatalytic activity. *Chem-Eur J* 2014, **20**: 14763–14770.
[36] Wu AX, Zhu ZX, Wang XL, *et al*. High-performance ZnO varistor ceramics prepared by arc-induced flash sintering with low energy consumption at room temperature. *High Volt* 2022, **7**: 222–232.